Supporting Information

Iyer-Biswas et al. 10.1073/pnas.1403232111

SI Text

1. Experimental Methods

1.1. Cloning of the Mutant Strain, FC1428. *C. crescentus* strain CB15 naturally adheres to surfaces via an adhesive polysaccharide termed a holdfast; production of holdfast requires the *hfsA* gene (1). Strain NA1000 is a laboratory-adapted relative of CB15 and bears a frameshift mutation in *hfsA*, rendering cells nonadhesive (2). We cloned the functional *hfsA(CB15)* allele into pMT-862 (3) and integrated it into the NA1000 chromosome at the *vanA* locus, under a vanillate-inducible promoter. The resultant strain, FC1428, only gains the ability to adhere to surfaces when exposed to vanillate. Cells are induced with 0.5 mM vanillate for 3 h before introduction into the microfluidic device; they are then allowed to adhere to the glass interior of the device. Vanillate-free media is then flowed over the cells for the remainder of the experiment; induction of *hfsA(CB15)* does not occur in newborn cells, which do not adhere and are thus washed out of the microfluidic chamber. This inducibly sticky strain allows for long experimental run times, as a constantly adherent strain would rapidly crowd the field of view with daughter cells produced over many generations.

1.2. Growth Protocol. For each experiment, individual colonies of FC1428 were selected from a fresh PYE-agar plate containing kanamycin (5 μg/mL) and grown overnight in PYE medium in a 30 °C roller incubator, taking care to ensure that the culture was in log phase. This culture was diluted to $OD_{660} = 0.1$ with fresh PYE and 0.5 mM vanillate and was induced for 3 h before being loaded onto the microfluidic channel in the previously temperature-stabilized chamber. PYE is a complex medium and its detailed composition is provided in ref. 4.

1.3. Microfluidic Device and Single-Cell Assay. See Fig. S1 for details of the microfluidics, optics, and image processing aspects of the experimental setup. Y-shaped microfluidic channels were fabricated and prepared as described in ref. 5. After thermal equilibration, the FC1428 bacterial cell culture was loaded into a single channel and incubated for 1 h. Typically enough cells stuck to the glass surface of the device after a 1-h period of incubation for the subsequent imaging experiment. The remaining cells (i.e., those that were not adherent) were then washed off in the laminar flow of the microfluidic device. Two computer-controlled syringe pumps (PHD2000, Harvard Apparatus) pumped thermally equilibrated PYE media through the channel at a constant flow rate (7 μL/min).

1.4. Time-Lapse Microscopy. The imaging process was automated such that the imaging, stage positioning, illumination, syringe pumps, and readout from the array detector were fully computer controlled and could operate autonomously throughout experiments of many days. Time-lapse single-cell measurements were performed on an inverted microscope (Nikon Ti Eclipse) equipped with a motorized sample stage and a controller (Prior Scientific ProScan III). Phase-contrast microscopy was performed with a Nikon Plan Fluor 100× oil objective, a 2.5× expander, and a mercury fiber illuminator (Nikon C-HGFI). A computer-controlled shutter (Lambda SC) was used to coordinate light exposure and image acquisition. The image was collected on an electron multiplying charge coupled device detector (EMCCD, Andor iXon+ DU888 1024 × 1024 pixels). To ensure thermal stability, the microscope and syringe pumps were enclosed by a home-made acrylic microscope enclosure (39” × 28” × 27”) heated with a closed-loop regulated heater fan (HGL419, Omega). A uniform temperature was maintained by a proportional integral derivative temperature controller (CSC32J, Omega) coupled with active airflow from two small-profile heater fans inside the enclosure. For experiments carried out below 20 °C, the temperature in the entire room was lowered to 6 °C and the aforementioned enclosure that includes the microscope was heated. Phase-contrast images of multiple fields of view were recorded at 1 frame per minute and the focus adjusted automatically using the built-in “perfect focus system” (Nikon PFS). A Virtual Instrument routine (LabView 8.6, National Instrument) was used to control all components (sample stage, autofocus, pumps, EMCCD, and shutter) and to run the experiment for extended periods of time (5–12 days).

1.5. Image Analysis and Construction of Growth Curves. The acquired phase-contrast images were processed by identifying each *C. crescentus* cell in MATLAB (MathWorks) and tracking the cells over time using custom code written in Python. The cross-sectional areas of each cell measured through a sequence of images were used to determine growth curves. From these data division events were identified. We chose to only include cells that divided for more than 10 generations in our subsequent analysis.

2. Cell Size Determination and Precision

Typical Gram-negative bacteria have cylindrical rotational symmetry around their anterior–posterior axes. In *C. crescentus*, the symmetry is around a curved axis because the cells are crescent shaped. As shown in Fig. S3, we have verified that the growth of the cell is predominantly along the longitudinal direction, by evaluating the curved midcell axis (the bisector of the observed area of the cell); this length itself grows with the same exponential growth rate as we deduce from the area. However, quantifying cell size by the straight-line length joining the anterior–posterior extremities of the cell instead would lead to an accumulation of errors because it ignores the inhomogeneous width of the cell perpendicular to this line, in the plane of observation. We use area because it obviates this problem and affords us an order of magnitude better precision. We expect the area to reflect the volume faithfully because cells are cylindrically symmetric and their lengths grow exponentially with the same time constant as the area.

Using a combination of thresholding the absolute intensity and ridge detection algorithms, the (pixellated) boundary of each cell was identified, frame by frame. Cell area was quantified by counting the total number of pixels inside the boundary for each cell in each frame. We compute the precision of our measurements in several different ways. First, we vary the threshold for cell edge detection over a 10% range ($\pm 5\%$ of the value used for all image analysis) and find that the area of each cell is changed by ∼2% at the beginning of each cell cycle; this number decreases further as the cell grows. Second, we perform control experiments with more frequent sampling (30 frames per minute) and use bootstrapping methods to estimate the error bars on the precision of our single-cell measurements in our experiments, which are performed at 1 frame per minute. Third, we examine the fluctuation in the areas of cells that do not grow during the course of the experiment but are not dead (a condition that is controlled by the media), at 1 frame per minute. The measurement uncertainty of a single-cell area is <2%. Because

we obtain between 4,000 and 16,000 growth curves at each temperature, the ensemble-averaged mean area at a given instant of time has an uncertainty of <0.03%.

The division times are taken to be the minima of the area vs. time curves. We estimate that the error in division times is less than 2 min (twice the inverse frame rate). Because the coefficient of variation (ratio of the SD to the mean) of the division-time distributions at all temperatures is ≈0.13 (see the following section), the SE in the mean division times at each temperatures (with 4,000–16,000 points) is 0.01–0.03 min.

3. Determination That the Growth Law Is Exponential

3.1. Fitting Individual Trajectories. The Langevin model for stochastic exponential cell-size growth is given by Eq. **4** of the main text and is used to find the correct procedure for ensemble averaging the growth curves to obtain the time evolution of the mean cell size, i.e., the growth law(s). Upon integrating this equation,

$$e^{-\kappa(T)t/2}\sqrt{a(t;T)}-\sqrt{a(0;T)}=\frac{1}{2}\int_0^t dt' e^{-\kappa(T)t'/2}\eta(t'). \quad \text{[S1]}$$

Thus, the time evolution of the square of the ensemble-averaged mean of the square root of the size is exponential:

$$\left\langle\sqrt{a(t;T)}\right\rangle^2=\left\langle\sqrt{a(0;T)}\right\rangle^2 e^{\kappa(T)t}. \quad \text{[S2]}$$

Using this result, at each temperature we fit the growth data for each generation, $\sqrt{a(t;T)}$ vs. t, with the best exponential fit, to find $\kappa/2$ and thus κ.

Because the mean and SD of the growth rates and division times evaluated by considering different generations of the same cell were equal to the same quantities evaluated across different cells at a given generation, the ergodic condition that ensemble averaging equals generational averaging holds for these data. Therefore, we do not see a systematic change in the reproductive output of a given cell from generation to generation, under these growth conditions.

A related issue is that of intergenerational correlations in these quantities. We find that there is a small but observable anticorrelation between the initial size of the cell and its division time at the end of that generation (but no correlation between the initial size and the growth rate) at all temperatures. This mild anticorrelation serves to restore the (absolute) size of a cell to the ensemble average and prevents "runaway" cells, i.e., larger (smaller) than average cells from getting progressively larger (smaller), compared with the ensemble mean, due to noisy relative size thresholding at division.

3.2. Distinguishing Between Functional Forms. Which functional form best fits the ensemble-averaged mean growth law, i.e., the increase of mean cell size with time in balanced growth conditions, has been debated. The two main contenders are the linear and exponential forms (6–9).

An important reason why ascertaining the growth law, beyond a reasonable doubt, has been an experimental challenge is because extraordinary (statistical) precision is required to distinguish an exponential from a straight line when each growth period is less than the time constant of the exponential. This can be seen by estimating the minimum precision required for discriminating between the two functions, by considering the geometrical aspects of exponential and linear curves for a given mean growth period $\langle\tau\rangle$, and a relative division threshold $\theta\equiv\langle a(\tau)\rangle/\langle a(0)\rangle$ (10) [Fig. 2*B* (main text) and Fig. S7]. The time at which the exponential curve deviates most from the straight line is then found to be

$$\tau_m=\langle\tau\rangle\frac{1}{\ln\theta}\ln\left[\frac{\theta-1}{\ln\theta}\right]. \quad \text{[S3]}$$

The maximal difference between the predicted sizes for the exponential and linear models (Δa_{max}) is thus the difference between the sizes predicted using each model at time τ_m:

$$\Delta a_{max}=\langle a(0)\rangle\left[1+(\theta-1)\left\{\frac{\tau_m}{\langle\tau\rangle}-\frac{1}{\ln\theta}\right\}\right]. \quad \text{[S4]}$$

Thus, the minimum precision of measurement required to distinguish between these models is determined by whether $\Delta a_{max}\gg\sigma(\tau_m)$ or not, where $\sigma(t)$ is the SD in a observed at time t. Scaling Δa_{max} by the predicted size at τ_m for the exponential model and defining $f(\theta)\equiv(\theta-1)/\ln\theta$, we thus arrive at the minimum precision required for distinguishing between the two models.

$$\begin{aligned}\text{minimum precision}&=\frac{\langle a(0)\rangle\langle\tau\rangle[1+f(\theta)(\ln(f(\theta))-1)]}{\langle a(0)\rangle[\langle\tau\rangle+\tau_m(\theta-1)]}\\&=\frac{1+f(\theta)[\ln(f(\theta))-1]}{1+f(\theta)\ln(f(\theta))}.\end{aligned} \quad \text{[S5]}$$

The required precision is ≈4% for a division size ratio of $\theta=1.8$, as is observed in our experiments. Because error in our mean area measurements is less than 0.03%, we can indeed unequivocally distinguish between exponential and linear growth.

To quantify the goodness of fit for both the exponential and linear fits, and to establish that the statistically preferred model is the exponential one, we use the following prescription. We recall that the ensemble-averaging procedure that correctly accounts for the cancellation of the noise contribution from $\eta(t)$, for the model of stochastic growth proposed, is to find the root-mean-square of the area $\langle\sqrt{a(t)}\rangle^2$ at each observation time (a noise model with additive noise or linear multiplicative noise is contradicted by the scaling of cell-size distributions observed). In this ensemble-averaging procedure, no ad hoc subtraction of or division by the initial size to de-trend the noise is necessary. If the growth law were linear rather than exponential, then $\langle\sqrt{a(t)}\rangle^2$ should fit better to a model that is of the form $ct+d$, where c and d are parameters of the linear model. The exponential fit has $\chi^2\approx 50$ for all temperatures (Table S1), compared with $\chi^2\approx 1,000$ for the best linear fits (Table S1). Because both models, exponential and linear, have the same number of degrees of freedom, two fitting parameters each (i.e., the mean initial size and the mean growth rate), the Akaike information-theoretic criterion index (AIC) (11) for each is simply given by its respective χ^2-value. Clearly the χ^2-value for the exponential model is much smaller than that for the linear growth model. However, we can use the AIC to determine the relative likelihood that the linear model is the correct description of data, not the exponential. Using $\exp[(\mathrm{AIC}_{exp}-\mathrm{AIC}_{\mathrm{lin}})/2]$, we find that it ranges from 10^{-70} to 10^{-500} for the different temperatures (the variability in the value coming from the differences in total numbers of growth curves at each temperature). Therefore, statistical measures of model selection overwhelmingly favor the exponential form.

We note that the residuals for the exponential fit in Fig. S5*C* have additional structure, not fully explained by a model that assumes a constant (time-independent) mean growth rate. We believe that the systematic behavior in the residual for the exponential fit suggests that there may be a small growth phase (cell age) dependence to the growth rate, reflecting specific underlying growth–division processes, such as restructuring of the cell for formation of end caps and the constricting of the division plane; this is an interesting avenue for future inquiry. Here, we have used the constant growth rate model because it is the most economical model to explain the

overwhelming majority of observations. We thus conclude that the growth law for these cells, under the conditions described in the text, is exponential.

We note that a formal comparison with other growth laws is also possible. The exponential fit compares favorably with a quadratic function (the simplest higher-order polynomial) too. Geometric considerations similar to those detailed above indicate that the minimum precision required to discriminate between exponential and quadratic growth laws is ≈0.1%, which is within our statistical precision. The best fits for the quadratic have coefficients for the quadratic term that are approximately equal (within a factor of 1.2–1.5 times) to the quadratic coefficient of the series expansion of the exponential function. To quantify the statistical significance of the goodness of each fit, we have used the Bayesian information criterion (BIC) (12), a common information-theoretic measure for weighing models with different numbers of fitting parameters (the quadratic has one additional free parameter over the exponential). The BIC for the quadratic fit is greater than that for the exponential by more than 11, which is very strong evidence against the quadratic. In summary, the quadratic fit is comparable in quality to the exponential fit but has an additional free parameter, and we thus favor the exponential.

4. Fitting the Data

4.1. Mean Division Times. The mean values of the division times at 34, 31, 28, 24, and 17 °C are 56, 72, 76, 98, and 201 min, respectively. In the main text we show that, if the individual rates of the Hinshelwood cycle exhibit an Arrhenius temperature dependence (in general, with different activation energies), the overall growth rate (equal to the geometric mean of the individual rates) varies similarly with temperature, with an effective activation energy equal to the arithmetic mean of the individual barrier heights. The argument can be generalized to other functional forms for the temperature dependence of the mean growth rate (or division rate). Specifically, if the individual rates instead follow the Ratkowsky form, $k_i(T) \sim (T - T_0)^2$ (13, 14), where T is absolute temperature and T_0 is a parameter of the empirical relation, we find by calculating the geometric mean of the individual rates that the overall growth rate $\kappa(T)$ has the following temperature dependence:

$$\kappa(T) = T^2\left[\left(1 - \frac{\langle T_0\rangle}{T}\right)^2 - \frac{\sigma_{T_0}^2}{T^2} + \mathcal{O}\left(\frac{1}{T^3}\right)\right] \qquad \text{[S6]}$$

$$\approx (T - \langle T_0\rangle)^2. \qquad \text{[S7]}$$

Thus, provided that the SD of the individual values of T_0 is small compared with their mean value, to leading order, the effective growth rate also scales as a Ratkowsky form, with the effective minimum temperature parameter equal to the arithmetic mean of the individual values, irrespective of the number of steps in the Hinshelwood cycle, up to leading order in temperature. We note that no restriction on ΔE_i is required for Eq. **3** of the main text to hold in the Arrhenius case.

4.2. Size Distribution. The distribution of cell sizes, under balanced growth conditions, is predicted to be a gamma distribution (15). We rescale the initial size distributions at all temperatures by their mean values (note that these distributions undergo a scaling collapse and thus have the same shape), and the resulting scaled distributions collapse to a single gamma distribution with a mean of 1. The only parameter of the distribution left to be determined is the (dimensionless) shape parameter; the value that we obtain for it by fitting is 16. Thus, we obtain the mean-rescaled initial size distribution $P(\tilde{a}(0))$, where $\tilde{a}(0) \equiv a(0)/\langle a(0)\rangle$.

4.3. Division-Time Distribution. The first passage time distribution (i.e., the division-time distribution) for a cell that grows from an initial size $a(0)$ to when it reaches a multiple θ of its initial size $\theta a(0)$, is a beta-exponential distribution (15),

$$\mathcal{P}(\tau|\tilde{a}(0)) = \frac{\langle\kappa(T)\rangle e^{-\tilde{a}(0)\langle\kappa(T)\rangle\tau}\left(1 - e^{-\langle\kappa(T)\rangle\tau}\right)^{(\theta-1)\tilde{a}(0)}}{\mathrm{beta}[\tilde{a}(0), \tilde{a}(0)(\theta-1)]}, \qquad \text{[S8]}$$

where beta is the beta function. Note that θ, the multiple of the initial size to which each cell grows, was observed to be ≈1.76, on average (see main text and Fig. S7). The mean growth rate $\langle\kappa(T)\rangle$ is known from observations at each temperature (Table S1). Moreover, the initial size distribution $P(\tilde{a}(0))$ has also been determined (see above). Therefore, the division-time distribution,

$$\mathcal{P}(\tau) \equiv \int d\tilde{a}(0) P(\tilde{a}(0)) \mathcal{P}(\tau|\tilde{a}(0)), \qquad \text{[S9]}$$

can be computed at each temperature without any additional fitting parameters.

For the fit in Fig. 3*B* of the main text, we restricted ourselves to data within ±20% of the mean growth rate because events outside of this range correspond to biological phenomena not included in the simple model (which assumes a constant growth rate), such as cells that become filamentous. However, these outliers are included in the scatter plots in Fig. 2 *A* and *B*. The coefficient of variation (ratio of the SD to the mean) of the division time distributions at all temperatures in the Arrhenius range (17–34 °C) is ≈13%.

5. Scaling Behaviors Beyond the Arrhenius Range

As discussed in the main text, we have performed single-cell experiments at 37 °C and 14 °C, temperatures that are, respectively, higher and lower than the Arrhenius range ["normal temperature range" (16)] for the mean growth rate, to investigate scaling behaviors at these extreme physiological temperatures. We have obtained data for between 2,000 and 4,000 generations (growth curves) for both conditions. We find that the single-cell growth law remains exponential for both these temperatures (Fig. S10). The mean division time observed at 37 °C is 54 min and at 14 °C, 319 min; in contrast, if they had followed the Arrhenius law (Fig. S11*C*), these values should have been ≈44 min and ≈237 min, respectively. Thus, the division rate observed at both temperatures is significantly slower than predicted by the Arrhenius law. However, the mean growth rate (of surviving cells) slows down proportionally (Fig. S11*A*); as a result $\langle\tau\rangle$ and $\langle\kappa^{-1}\rangle$ continue to scale linearly with each other, as they do in the Arrhenius range. Moreover, the initial cell size remains proportional to the size of the cell at division even outside the Arrhenius range; at 37 °C the mean value of the relative size threshold is 1.8 at both temperatures (Fig. S11*B*). Further, the mean-rescaled division-time distribution from 14 °C undergoes the same scaling collapse as the remaining temperatures in the Arrhenius range (Fig. S11*D*) but the distribution at 37 °C is slightly more noisy with COV ≈15%. We believe that this additional stochasticity, compared with other temperatures, is related to the onset of cell mortality—we observe significant mortality at 37 °C and the increased filamentation rate at this temperature. In Fig. S9 we show that the survival probability $S(t)$ of a cell at 37 °C is an exponential function of time, $S(t) \sim e^{-\nu t}$. By fitting the observed survival distribution, we estimate that ν, the probability per unit time that a cell may die, is 7% per mean duration of a generation (54 min). The mean-rescaled cell-size distributions from different times, at both temperatures, undergo scaling collapses, as predicted by the SHC. We see an increase in the initial cell size at both extreme temperatures, compared with the temperatures in the Arrhenius range; at present, we do not have an explanation for this observation.

1. Smith CS, Hinz A, Bodenmiller D, Larson DE, Brun YV (2003) Identification of genes required for synthesis of the adhesive holdfast in *Caulobacter crescentus*. *J Bacteriol* 185(4):1432–1442.
2. Marks ME, et al. (2010) The genetic basis of laboratory adaptation in *Caulobacter crescentus*. *J Bacteriol* 192(14):3678–3688.
3. Thanbichler M, Iniesta AA, Shapiro L (2007) A comprehensive set of plasmids for vanillate- and xylose-inducible gene expression in *Caulobacter crescentus*. *Nucleic Acids Res* 35(20):e137.
4. Ely B (1991) Genetics of *Caulobacter crescentus*. *Methods Enzymol* 204:372–384.
5. Lin Y, Li Y, Crosson S, Dinner AR, Scherer NF (2012) Phase resetting reveals network dynamics underlying a bacterial cell cycle. *PLoS Comput Biol* 8(11):e1002778.
6. Cooper S (2006) Distinguishing between linear and exponential cell growth during the division cycle: Single-cell studies, cell-culture studies, and the object of cell-cycle research. *Theor Biol Med Model* 3:10.
7. Cooper S (1991) *Bacterial Growth and Division* (Elsevier, Amsterdam).
8. Ubitschek HE (1968) Linear cell growth in *Escherichia coli*. *Biophys J* 8(7):792–804.
9. Koch A (2001) *Bacterial Growth and Form* (Springer, Berlin).
10. Tzur A, Kafri R, LeBleu VS, Lahav G, Kirschner MW (2009) Cell growth and size homeostasis in proliferating animal cells. *Science* 325(5937):167–171.
11. Burnham KP, Anderson DR (2002) *Model Selection and Multimodel Inference: A Practical Information-Theoretic Approach* (Springer, New York).
12. Schwarz G (1978) Estimating the dimension of a model. *Ann Stat* 6:461–464.
13. Ratkowsky DA, Olley J, McMeekin TA, Ball A (1982) Relationship between temperature and growth rate of bacterial cultures. *J Bacteriol* 149(1):1–5.
14. Ratkowsky DA, Lowry RK, McMeekin TA, Stokes AN, Chandler RE (1983) Model for bacterial culture growth rate throughout the entire biokinetic temperature range. *J Bacteriol* 154(3):1222–1226.
15. Iyer-Biswas S, Crooks GE, Scherer NF, Dinner AR (2014) Universality in stochastic exponential growth. *Phys Rev Lett* 113(2):028101.
16. Ingraham JL, Maaløe O, Neidhardt FC (1983) *Growth of the Bacterial Cell* (Sinauer, Sunderland, MA).

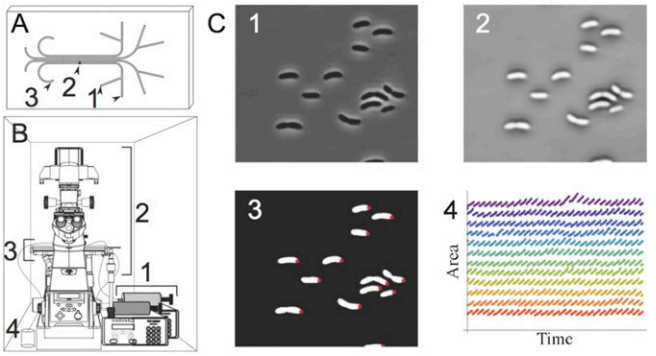

Fig. S1. Schematic of the experimental setup. (*A*) The microfluidic device (A1) creates a constant perfusion environment within the channel where imaging occurs (A2); there is continuous fluid exchange through the output (A3). It consists of four individual channels, which are connected to capillary tubing to create a sealed environment. Inputs of two different media may be connected at the upstream end. (*B*) The experimental apparatus. Each syringe is attached to a separate syringe pump to allow midexperiment switching between media (B1); images are obtained using a Nikon Ti-E microscope with autofocus (B2), which compensates for focal drift as the robotic XY stage holding the microfluidic device (B3) moves between multiple fields of view within the microfluidic channel during the course of long-term experiments. (B4). Each component is controlled by a custom LabVIEW program that completely automates the process of data acquisition after the experiment has been set up. (*C*) Image processing workflow. An example of the raw data (1,024 pixel × 1,024 pixel), a phase-contrast image, is shown in (C1). Each image is then processed with the goal of accurately and robustly detecting cell edges (C2). Features are then identified (C3): the processed images are thresholded to extract cell areas (white), and the point on each cell perimeter closest to the holdfast (red) is assumed to represent a near-stationary point and used to track cells (i.e., to maintain cell identity between every frame of the movie). A typical cell trajectory obtained with the above algorithm is shown (C4).

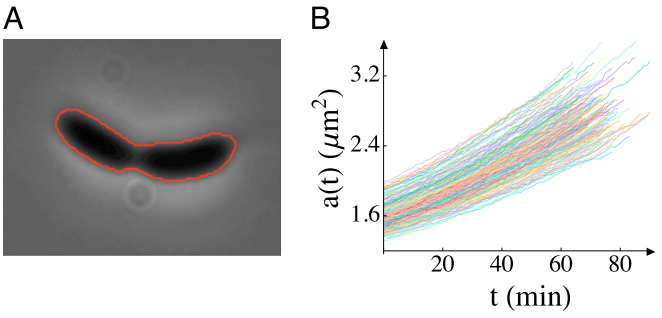

Fig. S2. From raw images to growth curves. Phase-contrast images such as the one shown in *A* are obtained for each field of view, for each time point, for an experiment at a given temperature. The pixellated boundary (shown in red) of each cell in each frame is extracted by custom image processing algorithms, which combine the absolute intensity level, the spatial gradients of the intensity levels, and a final thresholding step. By linking a sequence of processed images, we obtain area values as a function of time (*B*) for each generation of each cell. The curves in *B* are plotted with *t* set equal to 0 at the beginning of each generation. Data shown are from 5 cells (248 generations total) from an experiment performed at 31 °C.

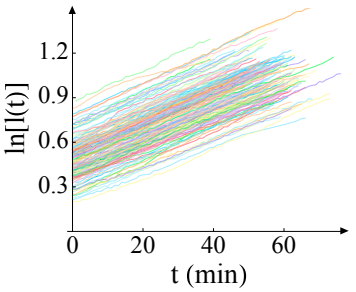

Fig. S3. Exponential growth of the longitudinal length of the cell. Data shown are from 5 cells (248 generations total) from an experiment performed at 31 °C. Here we see that $l(t)$, the longitudinal length of the cell, grows exponentially with time t as evidenced by the straight lines on the semilog plot shown. "ln" stands for the natural logarithm.

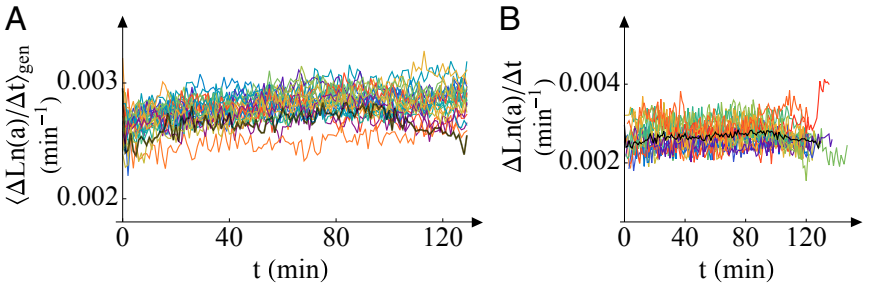

Fig. S4. Alternative representation of exponential growth. The rate of change of the logarithmic size is plotted as a function of time. For an exponential growth law, these curves should be parallel to the time axis, and the value of the vertical-axis intercept measures the growth rate κ for a cell. If the growth law were linear, the slope of this line should change by a factor of 2, which it does not. (*A*) Each color represents data from one stalked cell, averaged over all its generations. This averaging is denoted by $\langle \ldots \rangle_{gen}$. Data shown are from the experiment performed at 17 °C. Because the autocorrelation timescale in the growth curves was estimated to be ~15 min at this temperature, we consider time points separated by 20 min (>correlation time) to evaluate the change in the logarithmic size, so as to ensure statistical independence of successive points. (*B*) Averaging for a representative cell: we show the 20 generations that contributed to the black curve in *A*. "ln" denotes the natural logarithm.

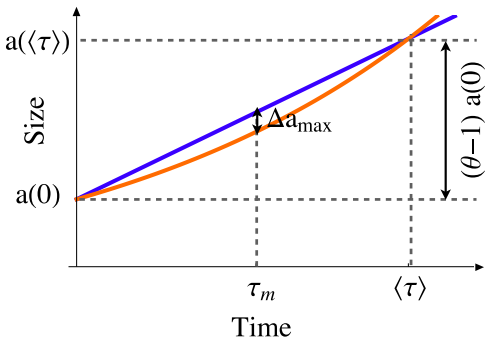

Fig. S5. Schematic illustrating the challenge of discriminating exponential and linear models. For a cell growing from an initial size, $a(0)$, to a multiple θ of the initial size, i.e., $\theta a(0)$, the linear (blue) and the exponential (red) fits (both passing through the initial and final points) maximally differ at a time τ_m and the magnitude of the maximal difference is Δa_{max}. The measurement precision has to be better than Δa_{max} for model selection (between linear and exponential) to be feasible. See *SI Text,* section 3.2 for discussion.

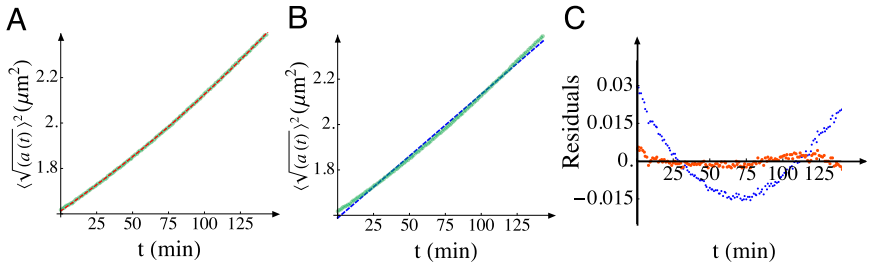

Fig. S6. Exponential vs. linear fits for the growth law. Experimental data (green) are fit by (*A*) red, exponential and (*B*) blue, linear functional forms. (*C*) Residuals for exponential (red) and linear (blue) fits of the root-mean-square growth curve for fits in *A* and *B*. Data are for 17 °C (~10,000 individual growth curves contributing). See *SI Text,* section 3.2 for discussion.

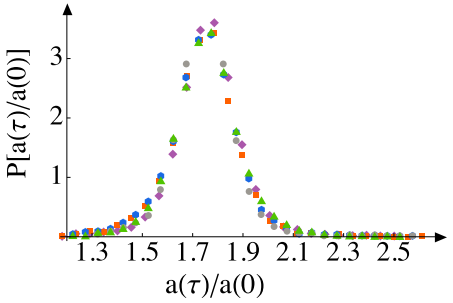

Fig. S7. Distributions of the relative size threshold at different temperatures. The probability distribution of the relative size increase of each cell at division, i.e., the ratio of size at division to initial size, $a(\tau)/a(0)$, is shown for all generations and all temperatures in the Arrhenius range (purple, 34 °C; green, 31 °C; orange, 28 °C; blue, 24 °C; gray, 17 °C). This plot shows that the distributions undergo a scaling collapse. The mean value is 1.76 and the COV is ~8%.

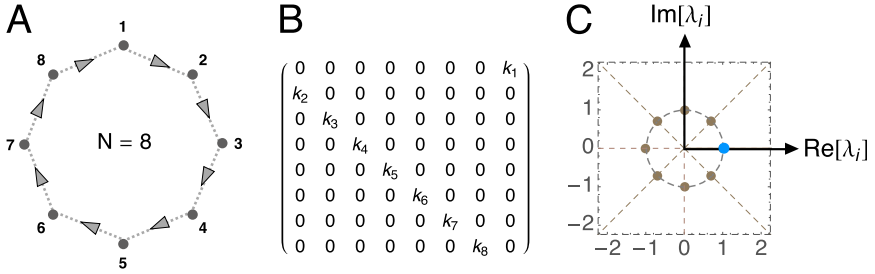

Fig. S8. The Hinshelwood cycle yields exponential growth with a rate equal to the geometric mean of constituent rates. Illustrative example with an $N=8$ Hinshelwood cycle (Fig. 4, main text). (*A*) Schematic reaction network corresponding to the cycle. (*B*) The rates can be collected in a matrix, $\mathbb{K}$. In this notation (15), each reaction $X_{i-1} \to X_{i-1} + X_i$ proceeds with rate $\sum_{j=1}^{N} \mathbb{K}_{ij}\, x_j$, where x_i is the copy number of species X_i, $\mathbb{K}_{ij} = k_i\, \delta_{i-1,j}$, and δ is the Kronecker delta; the index 0 is equivalent to *N*, closing the cycle. (*C*) The eigenvalues of $\mathbb{K}$ define the vertices of a regular polygon (here, an octagon, indicated by brown and blue filled circles) in the complex plane. The eigenvalues λ_i are obtained from the roots of the characteristic equation, $\det|\mathbb{K} - \lambda\, \mathbb{1}| = 0$, or equivalently $\lambda^8 = k_1 k_2 \ldots k_8$. Thus, there is always only one real positive root (blue), which has a magnitude equal to κ (15). This eigenvalue dominates the asymptotic dynamics and leads to exponential growth of all x_i with growth rate κ (Eq. **2**, main text).

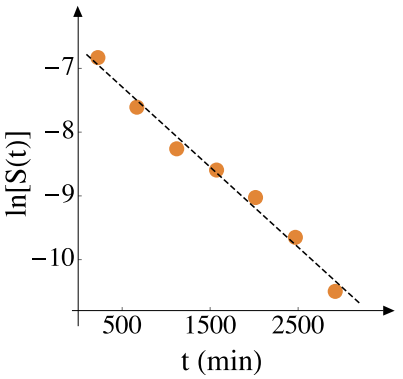

Fig. S9. Survival probability distribution at 37 °C. The survival probability $S(t)$ is observed to be an exponential distribution (straight line on a log-linear plot); $S(t) \sim e^{-\nu t}$, where ν is the probability per unit time that a cell dies, fits to 7% per mean duration of the generation of a cell (54 min). Data are from 241 cells. "ln" denotes the natural logarithm.

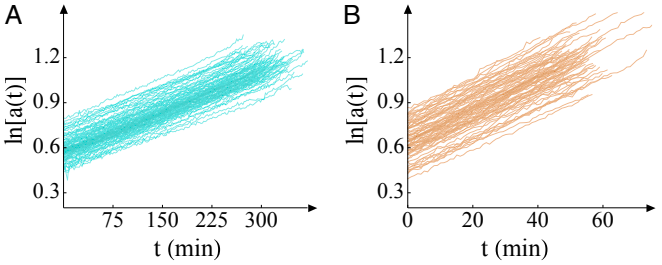

Fig. S10. Exponential growth at extreme temperatures. The single-cell growth law is observed to be exponential (for surviving cells) even at extreme temperatures: 14 °C (*A*) cyan and 37 °C (*B*) brown. Log-linear plots of the cell sizes as functions of time are shown. Growth data shown are for 80 generations for each condition. "ln" denotes the natural logarithm.

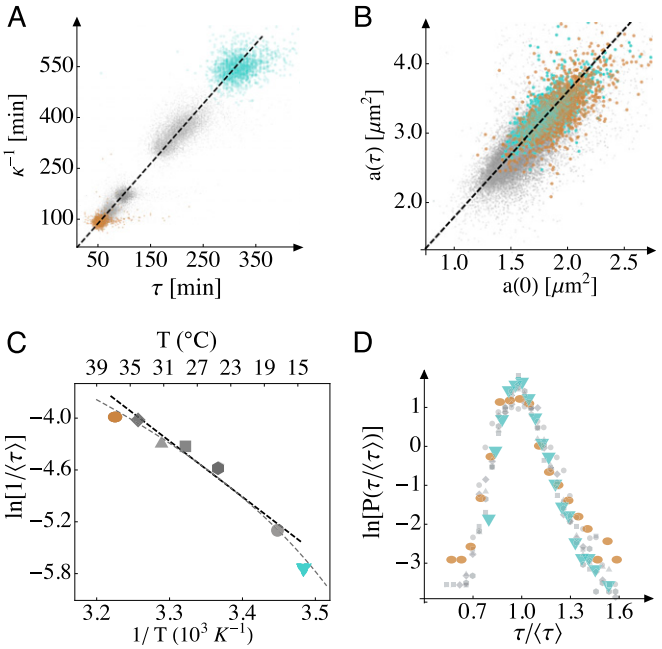

Fig. S11. Scaling behaviors at extreme temperatures. Data shown are from 14 °C (cyan) and 37 °C (brown), respectively, from 2,000 and 4,000 growth curves, with 50–200 time points each. Data from temperatures in the Arrhenius range are shown in gray for comparison (compare with Figs. 1–3 in the main text). (*A*) Linear scaling of the division timescale with the growth timescale; the slope of the best-fit line (dashed black) is 1.8. (*B*) Relative size thresholding of single cells; the slope of the best-fit straight line (dashed black) is 1.8. (*C*) Breakdown of Arrhenius scaling of the mean division rate, at extreme temperatures. The Arrhenius and Ratkowsky fits (Fig. 3*A*, main text) are shown for comparison. (*D*) The mean-rescaled division-time distributions at both these temperatures are superimposed on those from temperatures in the Arrhenius range. "ln" denotes the natural logarithm.

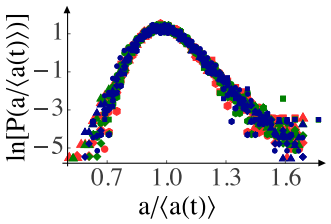

Fig. S12. Superposition of curves I (red), II (blue), and III (green) from Fig. 5*A*.

Table S1. Parameters and goodness of fit measures for exponential and linear models of growth

T(°C)	N_{ens}	$\left\{\langle\sqrt{a_0}\rangle^2(\mu m^2),\ \langle\kappa\rangle(min^{-1})\right\}$	$\left\{c(\mu m^2), d(min^{-1})\right\}$	χ^2_{exp}	χ^2_{lin}	Improbability index
17	9,634	{1.6,0.0028}	{1.6,0.005}	50	2,200	1.0×10^{-500}
24	4,224	{1.7,0.0058}	{1.6,0.012}	52	1,200	1.0×10^{-200}
28	4,769	{1.6,0.0075}	{1.6,0.015}	56	1,300	1.0×10^{-300}
31	15,240	{1.6,0.0078}	{1.6,0.015}	51	1,900	1.0×10^{-400}
34	13,340	{1.6,0.0099}	{1.6,0.019}	32	1,400	1.0×10^{-300}

Columns are temperature, T(°C), the number of growth curves, N_{ens}, the exponential model fit parameters $\{\langle\sqrt{a_0}\rangle^2(\mu m^2),\langle\kappa\rangle(min^{-1})\}$, the linear model fit parameters, $\{c\ (\mu m^2), d\ (min^{-1})\}$, the χ^2 value for the exponential fit, the χ^2 value for the linear fit, and the improbability index for the linear fit.